J. Fluid Mech. (2010), *vol.* 660, *pp.* 475–498. © Cambridge University Press 2010
doi:10.1017/S0022112010002764

Dynamics of sheared inelastic dumbbells

K. ANKI REDDY[1], J. TALBOT[2] AND V. KUMARAN[1]†

[1]Department of Chemical Engineering, Indian Institute of Science, Bangalore 560012, India

[2]Laboratoire de Physique Théorique de la Matiére Condensée, CNRS UMR 7600, Université Pierre et Marie Curie, 4, Place Jussieu, 75252 Paris Cedex, France

(Received 25 September 2009; revised 4 May 2010; accepted 11 May 2010; first published online 16 August 2010)

We study the dynamical properties of the homogeneous shear flow of inelastic dumbbells in two dimensions as a first step towards examining the effect of shape on the properties of flowing granular materials. The dumbbells are modelled as smooth fused disks characterized by the ratio of the distance between centres (L) and the disk diameter (D), with an aspect ratio (L/D) varying between 0 and 1 in our simulations. Area fractions studied are in the range 0.1–0.7, while coefficients of normal restitution (e_n) from 0.99 to 0.7 are considered. The simulations use a modified form of the event-driven methodology for circular disks. The average orientation is characterized by an order parameter S, which varies between 0 (for a perfectly disordered fluid) and 1 (for a fluid with the axes of all dumbbells in the same direction). We investigate power-law fits of S as a function of (L/D) and $(1 - e_n^2)$. There is a gradual increase in ordering as the area fraction is increased, as the aspect ratio is increased or as the coefficient of restitution is decreased. The order parameter has a maximum value of about 0.5 for the highest area fraction and lowest coefficient of restitution considered here. The mean energy of the velocity fluctuations in the flow direction is higher than that in the gradient direction and the rotational energy, though the difference decreases as the area fraction increases, due to the efficient collisional transfer of energy between the three directions. The distributions of the translational and rotational velocities are Gaussian to a very good approximation. The pressure is found to be remarkably independent of the coefficient of restitution. The pressure and dissipation rate show relatively little variation when scaled by the collision frequency for all the area fractions studied here, indicating that the collision frequency determines the momentum transport and energy dissipation, even at the lowest area fractions studied here. The mean angular velocity of the particles is equal to half the vorticity at low area fractions, but the magnitude systematically decreases to less than half the vorticity as the area fraction is increased, even though the stress tensor is symmetric.

Key words: granular media

1. Introduction

In the flowing state, granular materials form an important class of non-equilibrium-driven systems in which energy is dissipated in inelastic particle interactions. Since the grains are of macroscopic size, the energy due to thermal fluctuations is vanishingly small. Therefore, the grains can be maintained in a fluidized state only if there is a

† Email address for correspondence: kumaran@chemeng.iisc.ernet.in

continuous source of energy. One possible mechanism of energy production, which is studied in this paper, is internal production of energy due to mean shear. A balance between shear production and inelastic dissipation creates a homogeneous steady state, where the volume fraction and the granular 'temperature' are constant, and the velocity profile is linear. Unlike the case of granular materials driven by vibration at the boundaries, the steady state created in this manner is homogeneous and spatially uniform, and is therefore more amenable to detailed statistical analysis. Shear-driven flows are also encountered in practical applications such as rock slides and avalanches in geophysical applications, and chute flows in industrial applications.

Most experimental and theoretical studies of granular materials have considered systems composed of spherical particles, primarily because they are simpler than non-spherical ones. However, in real applications, asphericity is always present to some degree; it can be slight, as in the small asperities of steel balls, or large, as in grains of rice. An open issue is whether it is possible to apply granular flow theories constructed for spherical particles to real systems, since the theories do not incorporate the orientational degrees of freedom present in aspherical particles. Here, our objective is to examine the effect of shape on the dynamical properties of flows of two-dimensional dumbbells, which are a simple example of non-spherical particles. The dumbbells consist of two fused disks with their centres separated by distances upto one sphere diameter. We use a hard-particle model, where the pair potential is infinite when particles overlap, and zero otherwise. In this model, particles interact via instantaneous collisions, and since the collision time is zero, the probability of simultaneous three-particle interactions is vanishingly small compared to that of binary collisions.

It should be noted that the hard-particle collision model is an approximation, which is valid when the duration of an interaction is small compared to the time between successive particle interactions. Real particles have a finite stiffness, which results in deformation upon impact. These are usually modelled by linear or Hertzian spring–dashpots (Cundall & Strack 1979), in which the spring constant depends on the elasticity modulus and the size of the particles. The Hertzian model is suitable for smooth particles, since it accounts for the increase in the area of contact upon deformation. However, recent experiments (Cole & Peters 2007, 2008) have shown that the linear model is suitable for particles with asperities, where the initial resistive force is due to the compression of asperities. The spring constant for sand particles is in the range of $k_n = 0.2\text{–}2 \times 10^6\,\mathrm{N\,m}$ in the experiments; similar magnitudes can be expected for other types of particles such as glass beads or rice grains. The time of a collision can be estimated as $\tau_c = (1/\sqrt{k_n/m})$, where m is the mass of a particle. For particles with $k_n = 10^6\,\mathrm{N\,m}$, an effective diameter of the order of 1 mm and density $2500\,\mathrm{kg\,m^{-3}}$ (e.g. sand), we estimate the period of a collision $\tau_c \sim 10^{-4}\,\mathrm{s}$. In a shear flow, the flow time scale is the inverse of the strain rate $\dot{\gamma}^{-1}$, and the time between interactions can be estimated as $\dot{\gamma}^{-1}$, which is roughly the time taken for two particles separated by one particle diameter in the gradient direction to pass each other. A comparison of these two indicates that the binary collision approximation is valid for $\dot{\gamma} \ll 10^4\,\mathrm{s^{-1}}$ for moderately dense systems. The above estimation will fail at very high densities near the jamming limit, where a pair of particles collide many times within the time taken to translate past each other, but is valid for the low and moderately high densities considered here.

Since the time period of a collision is much smaller than the strain rates of interest in real granular flows, it is preferable to use an event-driven (ED) algorithm for hard particles, where the collisions are treated as instantaneous events. It is not efficient to

use molecular dynamics simulations where the particle stiffness k_n is made sufficiently high. This is because the time period of an interaction, which is proportional to $(1/\sqrt{k_n/m})$, decreases as the spring stiffness increases. Since the time step in the simulation has to be small compared to the period of interaction, this increases the computation time significantly in force-based molecular dynamics simulations. For this reason, an ED simulation procedure is used in the present analysis.

Some simulation and experimental studies have examined the dynamics of dense systems of non-spherical particles contained in cylinders under vertical or horizontal vibration (Villarruel *et al.* 2000; Lumay & Vandewalle 2004). Stokely, Diacou & Franklin (2003) investigated the two-dimensional packing of extremely prolate (aspect ratio $L/D = 10$) granular materials, comparing experiments with Monte Carlo simulations. A density-dependent nematic- to smectic-like transition was observed for vibrated granular rods (Blair, Neicu & Kudrolli 2003). Also, a density-dependent isotropic–nematic transition, consistent with theory and simulation, has been found for vibrated rod-shaped granular materials confined to quasi-two-dimensional containers (Galanis *et al.* 2006). Narayan, Ramaswamy & Menon (2007) presented experimental evidence for giant number fluctuations in a monolayer of fluidized rods, although similar behaviour has also been observed in systems of spherical particles (Aranson *et al.* 2008). All of these studies were carried out in boundary-driven systems, where the energy supply is due to vibration at the boundaries.

There have been some studies related to the simulations of granular flows of non-spherical particles, mostly using the soft-particle discrete-element method (DEM) developed by Cundall & Strack (1979). Here, the particles are allowed to overlap slightly, and the inter-particle force is a function of the distance of overlap between the particles. Gallas & Sokolowski (1993) and Bertrand, Leclaire & Levecque (2005) formulated a model where a non-spherical particle is replaced by a collection of spherical particles. Cleary & Sawley (2002) and Langston *et al.* (2004) developed a computation procedure for determining contact between the two given irregular shaped particles, but this was found to be computationally expensive. More references related to the contact force models of non-spherical particles can be found in Zhu *et al.* (2007). There are some studies (Poschel & Buchholtz 1995; Matuttis 1998) on the simulation of dense granular systems of non-spherical particles by describing overlapping particles with continuous interactions. Cleary (2008) studied the dense shear flow of non-spherical particles in a Couette cell using soft-particle DEM simulations in the volume-fraction regime where there is continuous contact between the particles. He observed inhomogeneities in the volume fraction, the mean velocity and the granular temperature profiles, depending on the types of boundary conditions used at the walls, and shear localization. He also found that the shear modulus depends sensitively on shape. Pena, Garcia-Rojo & Herrmann (2007) studied, using soft-particle simulations, dense flows of polygonal particles with varying shapes subjected to shear. The particles are in continuous contact in these simulations, and the contact orientating for the transmission of stress is mainly governed by the orientation of the particles in the case of elongated particles. At large shear deformation, samples with elongated particles, independent of their initial orientation, reach the same stationary value for both shear force and void ratio. These studies showed that shear is localized in shear bands whose width depends on the particle shape.

In a previous paper, we (Reddy, Kumaran & Talbot 2009) studied a system in the opposite limit where there is instantaneous contact between particles under a carefully controlled shear flow generated using Lees–Edwards boundary conditions (Lees & Edwards 1992). In this system, the density and temperature are constant and the mean

velocity is a linear function of the coordinate in the gradient direction. We examined the orientational ordering in relation to the known behaviour of equilibrium systems composed of hard anisotropic particles. We quantified the ordering with an order parameter S that is equal to 1 in a perfectly orientationally ordered system and 0 in an infinite system with randomly orientated particles. We observed that S increases 'continuously' from small values to about 0.5 as the packing fraction is increased or the coefficient of restitution is decreased. We verified that the continuous increase is not simply an artifact of small system sizes by performing simulations using up to four times more particles.

The principal orientation direction, θ_p, was determined from the eigenvector of the orientation matrix, whose corresponding eigenvalue is S. Although there are relatively large error bars on θ_p at low packing fraction, it is clear that the particles are orienting along the extensional direction. At higher packing fractions, the particles tend to orient closer to the flow direction: the highest packing fraction studied $\theta_p \approx \pi/8$. We also computed the orientational distribution function, $P(\theta)$, for a range of systems parameters. Except at the highest packing fraction, this function is well described by a truncated Fourier expansion: $P(\theta) = 1/\pi + (2S/\pi)\cos(2(\theta - \theta_p))$.

In this paper, we provide further analysis of the orientational-order parameter and examine the dynamical properties of the systems and how they are affected by the alignment. The stresses and dissipation rate have a definite dependence on the strain rate due to the requirements of dimensional consistency. Since particle contacts are instantaneous, there is no material time scale in the system. Therefore, all time dimensions can be scaled by the inverse of the strain rate, and the strain rate can be set equal to 1 without loss of generality. From dimensional considerations, all components of the stress are proportional to the square of the strain rate (Bagnold law), and the dissipation rate scales as the cube of the strain rate.

The fluctuating velocities of the particles (granular temperature) are linked to the strain rate through the energy-balance condition, and the ratio of the strain rate and the square root of the granular temperature is related to the coefficients of restitution. The average orientation and the probability distribution of particle orientations depend only on the area fraction, the aspect ratio and the coefficient of restitution. We examine the dependence of the orientation on these parameters, and also the effect of aspect ratio on the Bagnold coefficients (ratio of stress and square of strain rate) and the dissipation rate. The simulation methodology is discussed in § 2, and the results for the orientation distribution, velocity and angular velocity distributions and stresses are reported in § 3. The results are briefly summarized in § 4.

2. Collision model and simulation methodology

Granular flows of hard spherical particles (particles in which the pair potential is infinite when there is overlap, and zero otherwise) have been simulated by the ED method. The ED method is used to simulate instantaneous collisions between hard particles, where the simulation proceeds in discrete collision events, instead of the fixed time intervals used in molecular dynamics for molecules with continuous potentials.

We employ the method of retrospective collision detection first proposed by Rebertus & Sando (1977). The method works by attempting to advance the configuration from t to $t + \Delta t$ in the following way. The position and orientation of each particle are updated from their values at t to time $t + \Delta t$, as though no

other particles were present. At the end of this step, overlaps between one or several pairs of particles may be present. (Of course, if overlaps are detected, in the actual dynamics collisions would have occurred somewhere between t and $t+\Delta t$.) For each overlapping pair, the collision equation is solved to find the time of collision. A list of these times is sorted in chronological order and secondary collisions are removed (for example, if particle i collides with particle j and then subsequently with k, the collision pair (i, k) is deleted from the list). For each remaining pair in the collision list, the program rewinds the position and orientation to the point of impact, implements the collision dynamics by calculating the post-collisional translational and angular velocities of each colliding particle and then advances the pair to the time $t+\Delta t$. Of course, the final configuration is invalid if overlaps are present in the system at time $t+\Delta t$. If this condition applies, the attempt is abandoned and the configuration is reset to its state at t. The time interval is then reduced to $\Delta t/2$ and the above procedure is repeated. If there is no overlap at $t+\Delta t/2$, the program attempts to advance the configuration from $t+\Delta t/2$ to $t+\Delta t$. If the new attempt to advance the configuration is unsuccessful, the time step is halved again, and so on. In this way, the program incorporates all collisions in the correct sequence (with the possible exception of a few grazing collisions that may be missed if the particles are highly anisotropic). The complicated (although not very time-consuming) part consists of handling multiple overlaps and resolving sequences of (possibly) inter-dependent collisions occurring within a very short time of each other.

For the algorithm to function efficiently, Δt must be well chosen: not too small so that the system evolves too slowly and not too large so that collisions cannot be resolved unambiguously or are missed. In fact, the algorithm is remarkably robust for the current system. It works for a wide range of packing fractions ($0.1 \leqslant \phi \leqslant 0.7$) and geometries ($0 \leqslant L/D \leqslant 1$). More details on the simulation procedure can be found in Allen, Frenkel & Talbot (1989).

The inelastic hard-disk model has been used extensively for spherical particles with a constant coefficient of restitution. We extended the collision equations to inelastic non-spherical particles as follows. Consider two dumbbells with linear velocities $\boldsymbol{v}_1$, $\boldsymbol{v}_2$ and angular velocities ω_1, ω_2. Then, the total pre-collisional relative velocity at contact is

$$\boldsymbol{g}_{12} = \boldsymbol{v}_{12} + \boldsymbol{\omega}_1 \times \boldsymbol{r}_{c1} - \boldsymbol{\omega}_2 \times \boldsymbol{r}_{c2}, \tag{2.1}$$

where $\boldsymbol{v}_{12} = \boldsymbol{v}_1 - \boldsymbol{v}_2$. During collision, the components of $\boldsymbol{g}_{12}$ change such that

$$(\boldsymbol{n} \cdot \boldsymbol{g}'_{12}) = -e_n(\boldsymbol{n} \cdot \boldsymbol{g}_{12})$$
$$(\boldsymbol{I} - \boldsymbol{nn}) \cdot \boldsymbol{g}'_{12} = (\boldsymbol{I} - \boldsymbol{nn}) \cdot \boldsymbol{g}_{12},$$

where $\boldsymbol{n}$ is the unit vector along the centreline of the two sphere segments in the dumbbell that are colliding and primed quantities denote values after collision. The parameter e_n is the normal coefficients of restitution. The linear and angular momentum change of the two particles in a collision can be written as,

$$\boldsymbol{p}'_1 = \boldsymbol{p}_1 + \Delta \boldsymbol{p}$$
$$\boldsymbol{p}'_2 = \boldsymbol{p}_2 - \Delta \boldsymbol{p}$$
$$\boldsymbol{J}'_1 = \boldsymbol{J}_1 + \boldsymbol{r}_{c1} \times \Delta \boldsymbol{p}$$
$$\boldsymbol{J}'_2 = \boldsymbol{J}_2 - \boldsymbol{r}_{c2} \times \Delta \boldsymbol{p},$$

where

$$\Delta p = \frac{-(1+e_n)\boldsymbol{g}_{12}\cdot\boldsymbol{n}}{2/m + (\boldsymbol{r}_{c1}\times\boldsymbol{n})^2/I + (\boldsymbol{r}_{c2}\times\boldsymbol{n})^2/I}, \tag{2.2}$$

where I is the moment of inertia and $\Delta\boldsymbol{p} = \boldsymbol{n}\Delta p$. The case $e_n = 1$ corresponds to perfectly smooth elastic particles, where the component of the relative velocity along the line joining the centres of the particles is reversed in a collision. The kinetic energy of the particles is unchanged in a collision for $e_n = 1$, while there is a dissipation of energy for $e_n < 1$. In a steady shear flow, there is a production of energy due to the mean shear, and a system of elastic particles will heat up because there is no energy dissipation. A steady state is usually generated by applying a thermostat on the system. In a granular fluid, there is energy dissipation due to inelastic collisions, and a steady state is generated where there is a balance between the shear production and the dissipation due to inelastic collisions.

We generate homogeneously sheared inelastic hard dumbbell configurations with a particular L/D ratio, where L is the distance between the centres of the fused disks of a dumbbell and D is the diameter of the disk, using the Lees–Edwards boundary conditions (Lees & Edwards 1972). The simulation box dimensions, l_x and l_y, are both are of unit length. In our simulation geometry, x and y are the velocity and velocity-gradient directions, respectively. The top and the bottom boxes move with velocities $+U$ and $-U$, respectively, with respect to the central box. When a particle crosses the top/bottom boundary of the central box with a horizontal velocity v_x, its image enters through the bottom/top with a horizontal velocity $(v_x)_{image} = v_x \mp U$. This induces shear at the top/bottom boundaries of the central box, which then propagates by collisions into the central box. For most of the results reported here, the number of dumbbells used is 216; however, we have checked system-size dependence by carrying out some simulations with four times the box size and 864 dumbbells, and find no significant variation between the larger and smaller systems. The dumbbell configuration and snapshots of the simulation box at different area fractions are shown in figures 1 and 2, respectively.

If the system is homogeneously sheared, a linear-velocity profile with a shear rate $v_x = (\dot{\gamma}\, y)$ is expected to be induced in the central box, and the area fraction, the angular velocity and the stress tensor are expected to be constant. These dynamical variables are extracted by dividing the channel into 10 bins of equal width and averaging over all the particles within one bin. With this procedure, we average over 500 realizations for the average value for each bin, and each bin contains about 20 particles on average. Therefore, the averages are calculated over approximately 10^4 particles for each data point across the channel. In the simulations, we find a constant area fraction and a linear mean-velocity profile to a very good approximation, as shown in figure 3 for $(L/D) = 1.0$, $e_n = 0.8$ and for two different values of the area fraction. All the components of the stress tensor are also found to be a constant across the channel. There is a larger variation in the mean angular velocity across the channel, as observed in figure 3, and the variation has a maximum of about 20 % for $\phi = 0.1$. This type of variation in the angular velocity was observed for all the simulations carried out here, and the variation increased as $e_n \to 1$. This increase in the variation of the angular velocity is for the following reason. Since the temperature scales as $(\dot{\gamma}^2 D^2/(1 - e_n^2))$ from energy balance, the ratio of the magnitude of the velocity fluctuations and the local strain rate increases. In a similar manner, the ratio of the angular velocity fluctuations and the average angular velocity also increases, and the relatively small value of the average angular velocity is obtained by averaging

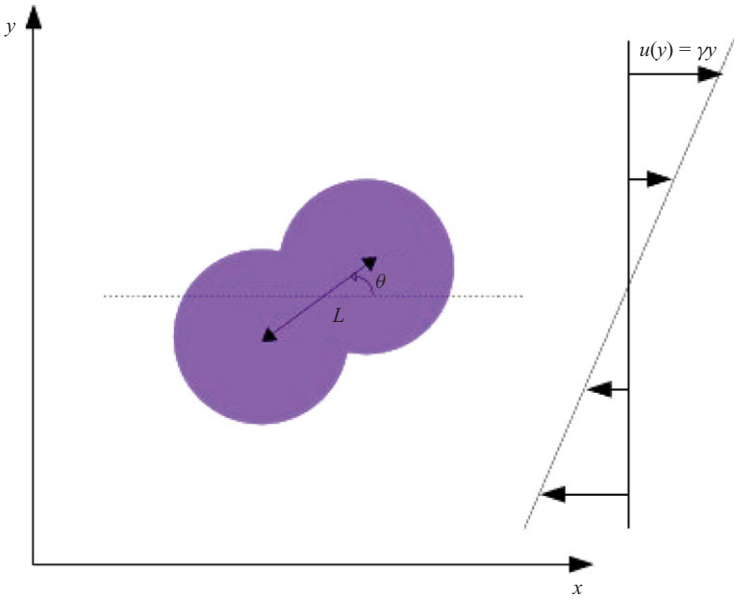

FIGURE 1. (Colour online) A dumbbell consists of two fused disks of diameter D with centres separated by a distance L. The Lees–Edwards boundary conditions induce a uniform shear in the sense shown. The orientation of the dumbbell with respect to the x-axis is denoted by θ.

over large fluctuating velocities. This results in poorer statistics for the angular velocity distributions. Surprisingly, we find that even when there are fluctuations in the angular velocity across the simulation cell, the mean velocity is very close to a linear-velocity profile and the stresses are constant. Therefore, when we report results for the angular velocity, we take care to show the error bars of width equal to two times the standard deviation of the angular velocity across the channel. Error bars are not reported for the stresses and the granular temperature, because these are numerically small.

3. Results and discussion

3.1. *Orientational order*

We define the orientation vector $\boldsymbol{u}_i$ of a particle ith as the unit vector in the direction of the line joining the centres of the two fused disks. The orientational order in the system was investigated using the matrix,

$$Q_{\alpha\beta} = \frac{1}{N}\left\langle \sum_{i=1}^{N} (2u_{\alpha i}u_{\beta i} - \delta_{\alpha\beta}) \right\rangle, \tag{3.1}$$

where $u_{\alpha i}$ denotes the component α of the unit vector specifying the direction of the ith dumbbell and the subscript $\alpha = x, y$ is used to denote vector directions. The angular brackets in (3.1) denote an average over a (large) number of configurations at equally spaced time intervals.

There are two orientational measures, which emerge from the matrix $Q_{\alpha\beta}$: the first is the degree of alignment S, and the second is the principal axis of alignment. The matrix Q has two eigenvalues, of which the largest, S, is the order parameter. In a perfectly orientationally ordered system $S = 1$, while in the isotropic phase (for an infinite system) $S = 0$. The matrix $Q_{\alpha\beta}$ also has two eigenvectors, which give the

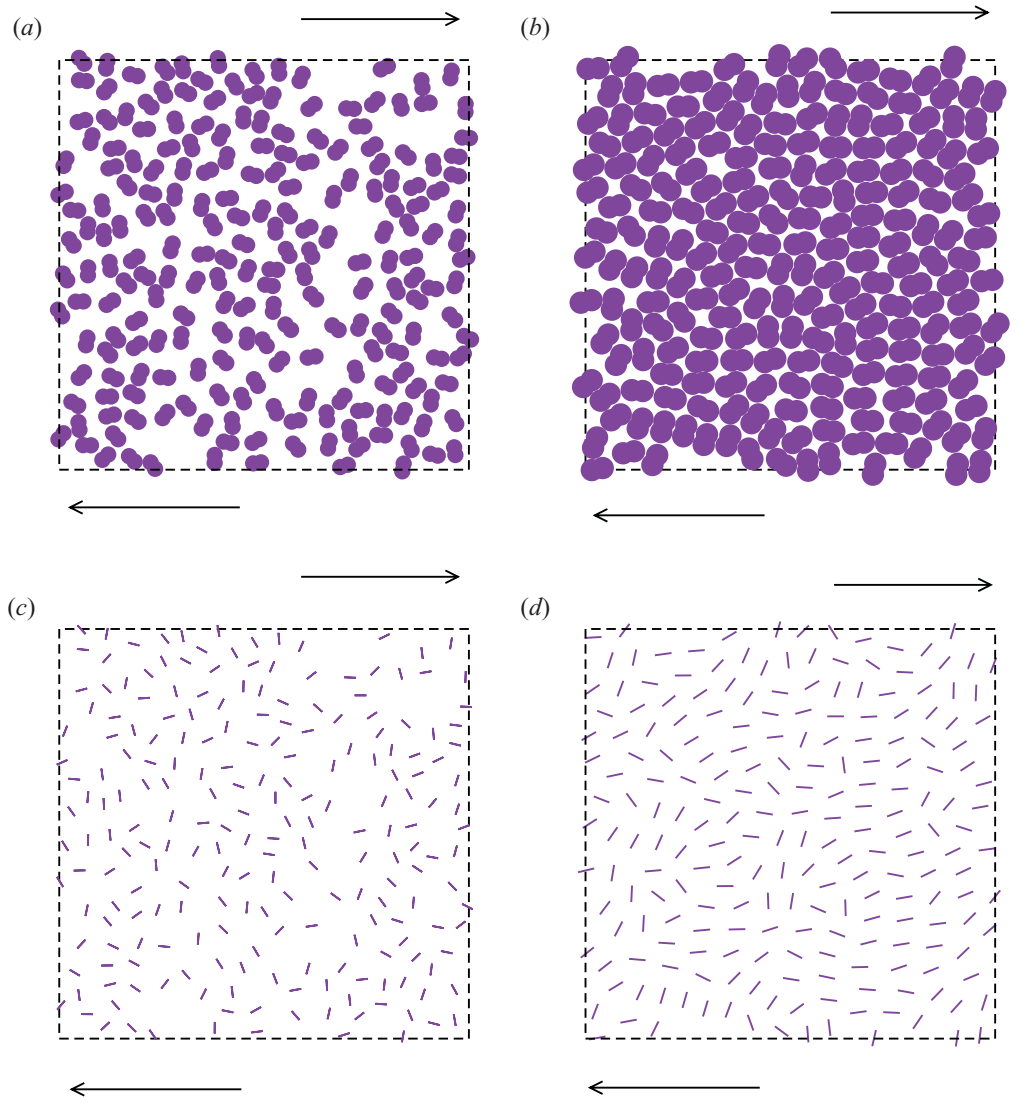

FIGURE 2. (Colour online) Snapshot of dumbbells at area fractions of (*a*) and (*c*) 0.4, and (*b*) and (*d*) 0.8. (*a*) and (*b*) The space-filling representation, while (*c*) and (*d*) the orientations.

principal axes of orientation. The eigenvector corresponding to the eigenvalue S is major principal axis, which is the direction along which the probability distribution of the orientation angles is a maximum.

In our simulations, each data point is obtained by averaging over 500 realizations of the system with 216 particles. Therefore, we average over approximately 10^5 samples. Using the central limit theorem, it can easily be inferred that the statistical error in the results for the order parameter is of the order of 3×10^{-3}. Therefore, we take care to analyse results only where the order parameter is greater than about 0.01, since order parameter values below this could be affected by sampling errors.

First we examine the order parameter as a function of area fraction for different L/D ratios. The order parameter is shown in figure 4 as a function of area fraction

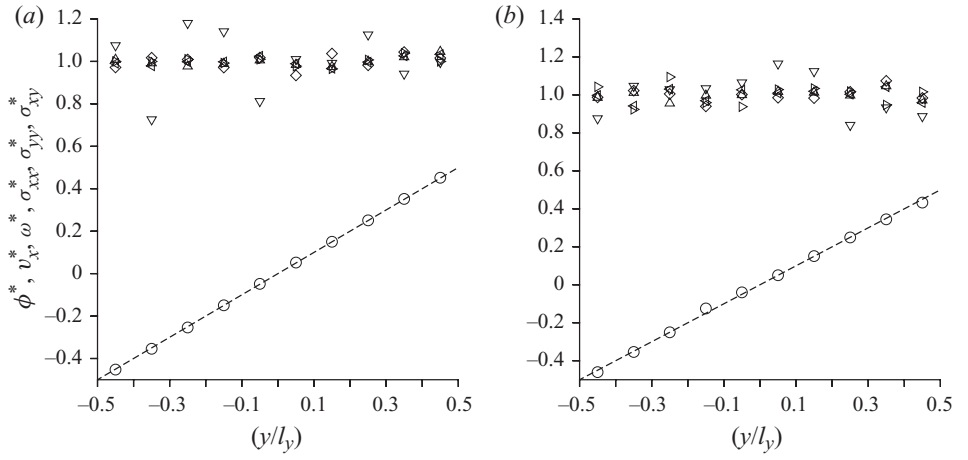

FIGURE 3. The average velocity $v_x^* = (v_x/\dot{\gamma} l_y)$ ($\bigcirc$), the scaled area fraction $\phi^* = (\phi/\bar{\phi})$ ($\triangle$), the scaled angular velocity $\omega^* = (\omega/\bar{\omega})$ ($\triangledown$), the scaled components of the stress $\sigma_{xx}^* = (\sigma_{xx}/\bar{\sigma}_{xx})$ ($\triangleleft$), $\sigma_{yy}^* = (\sigma_{yy}/\bar{\sigma}_{yy})$ ($\triangleright$) and $\sigma_{zz}^* = (\sigma_{zz}/\bar{\sigma}_{zz})$($\diamond$), as a function of distance across the channel $y^* = (y/l_y)$ for $(L/D) = 1$, $e_n = 0.8$ and for average area fraction $\phi = 0.1$ (a) and $\phi = 0.7$ (b). Here, l_y is the height of the simulation box, which has been divided into 10 equal bins, and the over bars represent averages over the entire box. The dashed line shows the expected linear-velocity profile $v_x^* = (y/l_y)$.

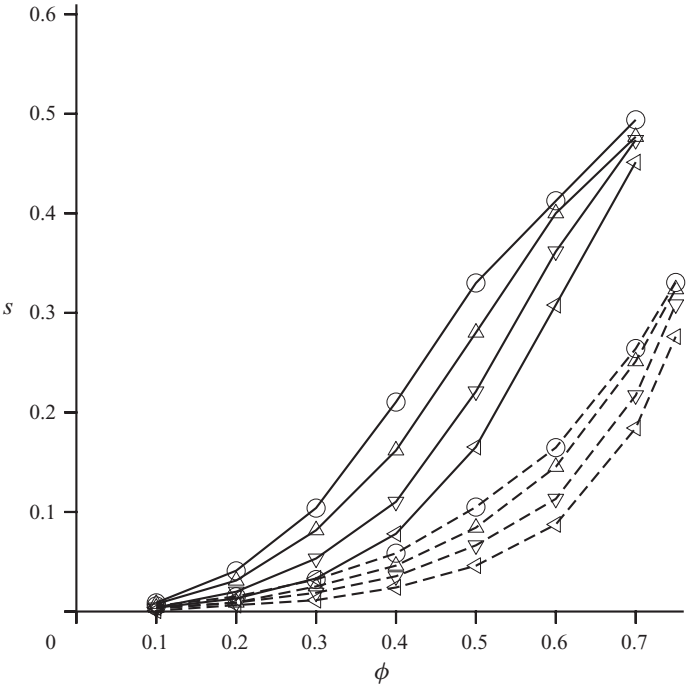

FIGURE 4. The order parameter S versus area fraction ϕ for $(L/D) = 0.25$ (dashed lines) and $(L/D) = 1.0$ (solid lines), and for coefficients of restitution $e_n = 0.7$ ($\bigcirc$), $e_n = 0.8$ ($\triangle$), $e_n = 0.9$ ($\triangledown$), $e_n = 0.95$ ($\triangleleft$) and $e_n = 0.98$ ($\triangleright$).

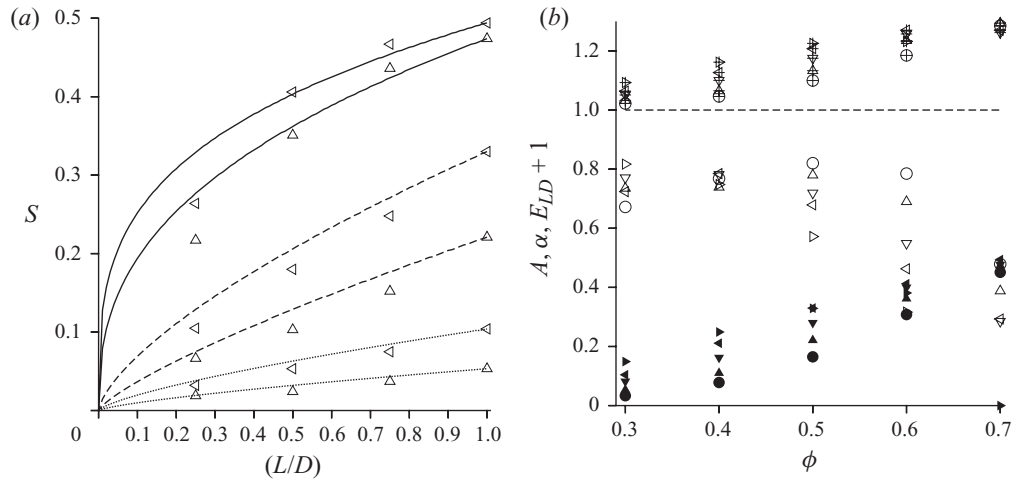

FIGURE 5. The order parameter S versus (L/D) (a) for $\phi = 0.3$ (dotted lines), $\phi = 0.5$ (dashed lines) and $\phi = 0.7$ (solid lines); and (b) the best-fit parameters A (open symbols) and α (filled symbols) in (3.2), and $E_{LD} + 1$ (symbols with superscribed plus) as a function of ϕ. The coefficients of restitution are $e_n = 0.95$ (○), $e_n = 0.9$ (△), $e_n = 0.8$ (▽), $e_n = 0.7$ (◁) and $e_n = 0.6$ (▷), and only results for $e_n = 0.9$ and $e_n = 0.7$ are shown in (a) for clarity.

for three different values of (L/D) and for different coefficients of restitution. An important result is that there is an increase in the ordering as the area fraction is increased or the coefficient of restitution is decreased, but the change is continuous. This is in contrast to a phase transition, where there is a discontinuous change in the order parameter. In order to ensure that the continuous increase is not an artifact of the finite system size (a first-order transition in a system of infinite extent could appear continuous in a finite size system), we have increased the system size by a factor of 4, and found that there is a change of less than 1 % in the value of S.

The increase in ordering with area fraction is easy to understand on the basis of packing constraints. Figure 4 shows that the order parameter increases as the square of the area fraction in the limit of low area fractions. (We have not included the data for $(L/D) = 0.005$ in figure 4 because the order parameter goes below 0.01 in the low-area-fraction limit, and the results there could be affected by errors due to finite sample size.) This is physically understandable, since we would expect the ordering to be induced by the biasing of binary collisions due to the mean shear in the limit of low area fraction; since the collisions frequency is proportional to ϕ^2 in the low-area-fraction limit $\phi \to 0$, we expect the order parameter also to be proportional to ϕ^2 in this limit.

The increase in ordering with the aspect ratio (L/D) is shown in figure 5(a). It is observed that the ordering increases as the aspect ratio increases. In the previous paper (Reddy *et al.* 2009), we assumed a linear dependence of S on L/D. Here, we examine a more general power-law form:

$$S = A(L/D)^{\alpha}. \tag{3.2}$$

The values of A and α are shown as a function of area fraction ϕ and e_n in figure 5(b). The best fits obtained using an equation of the form (3.2) are shown by the lines in figure 5(a). It is observed that α is close to 1 at relatively low area fractions, indicating that the order parameter is roughly proportional to (L/D). However, as the area fraction increases, the order parameter shows a slower increase with (L/D).

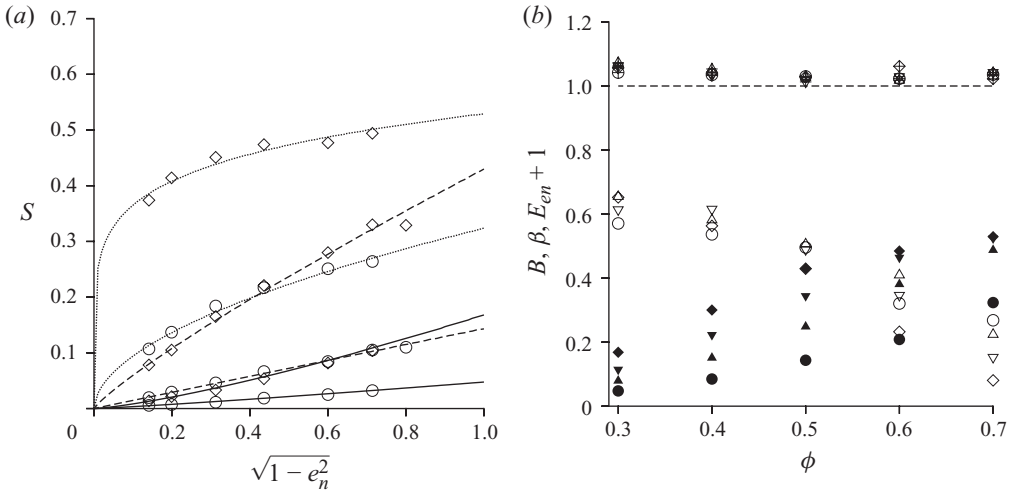

FIGURE 6. (*a*) The order parameter S as a function of $(1-e_n^2)^{1/2}$ for $(L/D) = 0.25$ (○) and $(L/D) = 1.0$ (◇) (filled symbols) and for packing fraction $\phi = 0.3$ (solid line), $\phi = 0.5$ (dashed line) and $\phi = 0.7$ (dotted line). The lines in (*a*) shows the best fits to (3.4), while the parameters B, β and $E_{en}+1$ are shown as a function of ϕ in (*b*) for $(L/D) = 0.25$ (○), $(L/D) = 0.5$ (◁), $(L/D) = 0.75$ (▽) and $(L/D) = 1.0$ (◇).

It should be noted that even at the highest area fractions and aspect ratios analysed here, the orientational order parameter has a maximum of about 0.5, far below the value of 1.0 for a perfectly aligned collection of rods.

Figure 5(*b*) also shows the standard deviation between the simulation result for S and the power-law fit 3.2, E_{LD}, which is defined as,

$$E_{LD} = \sqrt{\frac{\sum_{(L/D)} (S - A(L/D)^{\alpha})^2}{\sum_{(L/D)} S}}, \tag{3.3}$$

where the summation in the above equation is carried out for $(L/D) = 0.25, 0.5, 0.75$ and 1.0. Figure 5(*b*) shows $E_{LD}+1$, in order to separate the standard deviation from the results for α. It is observed that E_{LD} increases nearly linearly with area fraction, and it increases as the coefficient of restitution is decreased. The maximum value of E_{LD} is about 0.25 and the higher area fraction of 0.7.

The variation of the order parameter with the coefficient of restitution is shown in figure 6(*a*). The increase in ordering with inelasticity can be understood as follows. For a steady shear flow, there is a balance between the rate of production of fluctuating energy due to mean shear and the rate of dissipation due to inelastic collisions. We denote the mean square of the velocity fluctuations as T, the analogue of the granular temperature (the particle mass can be set equal to 1 without loss of generality). The rate of production of energy is proportional to the viscosity times square of the shear rate. For a fluid of hard particles, the viscosity is $(T^{1/2}/D)$ times a function of area fraction and aspect ratio. Therefore, the rate of production of fluctuating energy per unit area is $(T^{1/2}\dot{\gamma}^2/D)$. The rate of dissipation is proportional to $((1-e_n^2)T^{3/2}/D^3)$ times a function of the area fraction and aspect ratio, since the energy lost in a collision is $(1-e_n^2)T$ and the collision frequency per unit area is $(T^{1/2}/D^3)$. A balance

between these two indicates that $T \sim (D\dot{\gamma}/(1-e_n^2)^{1/2})^2$ times a function of the area fraction and aspect ratio. Therefore, if we vary coefficient of restitution at constant area fraction and aspect ratio, the fluctuating velocity decreases at constant shear rate. Since velocity fluctuations tend to randomize the system, whereas the mean shear tends to align particles in the flow direction, a decrease in the coefficient of restitution increases ordering in the system.

The variation of the order parameter with the coefficient of restitution for different aspect ratios and area fractions is shown in figure 6(*a*). An interesting feature of figure 6(*a*) is that the order parameter decreases to zero for $e_n \to 1$. Since the rate of shear production and inelastic dissipation are equal at steady state, and $\dot{\gamma} = ((1-e_n^2)T/D^2)^{1/2}$, the limit $e_n \to 1$ corresponds to an elastic system with no shear. In this case, figure 6(*a*) shows that there is no orientational ordering. Therefore, for all the (L/D) ratios and area fractions studied here, there is no spontaneous symmetry breaking and order/disorder transition in the absence of shear. The increase in ordering is only due to the imposition of a shear flow. For nearly elastic particles, figure 6(*a*) shows that the order parameter increases approximately as $(1-e_n^2)^{1/2}$. This is because, as explained earlier on the basis of an energy-balance argument, the ratio of the shear stress and the square root of temperature is proportional to $(1-e_n^2)^{1/2}$ in the limit $e_n \to 1$. Since the mean shear tends to align the particles, whereas the random fluctuations tend to increase disorder, we would expect $S \propto (1-e_n^2)^{1/2}$ for $e_n \to 1$. We attempt to obtain a power-law fit for the order parameter of the form,

$$S = B\left(1-e_n^2\right)^{\beta}. \tag{3.4}$$

The parameters B and β for the best fits for the order parameter are shown in figure 6(*b*), while the values of the order parameter obtained using a power-law fit are shown in figure 6(*a*). It is observed that $\beta \approx 0.5$ for low area fractions, as expected from the above arguments. However, β decreases as the area fraction increases.

Figure 6(*b*) also shows the standard deviation between the simulation result for S and the power-law fit (3.2), E_{LD}, which is defined as:

$$E_{en} = \sqrt{\frac{\sum_{e_n}\left(S - B\left(1-e_n^2\right)^{\beta}\right)^2}{\sum_{e_n} S}}, \tag{3.5}$$

where the summation in the above equation is carried out for five different values $e_n = 0.95, 0.9, 0.8, 0.7$ and 0.6. Figure 6(*b*) shows $E_{en} + 1$, in order to separate the standard deviation from the results for β. It is observed that E_{en} is numerically small for all values of area fraction and coefficient of restitution. We conclude that the power-law fit (3.4) is a good descriptor for the state of ordering in the system, even for coefficients of restitution as low as 0.6.

The orientational distribution function, $P(\theta)$, as well as the principal orientation direction, θ_p, are discussed in Reddy *et al.* (2009).

3.2. *Temperature and velocity distributions*

For a two-dimensional flow of non-circular particles, the temperature is defined as $T = (1/3)\langle v_x'^2 + v_y'^2 + I\omega'^2\rangle$, where $v_x' = (v_x - \langle v_x\rangle)$, $v_y' = v_y$ and $\omega' = (\omega - \langle\omega\rangle)$ are the fluctuating velocities, $\langle v_x\rangle$ is the (local) mean velocity and $\langle\omega\rangle$ is the angular velocity, which is a constant across the simulation box for a uniform shear flow. First, we discuss the expected variation of the temperature in the limit of low area fraction

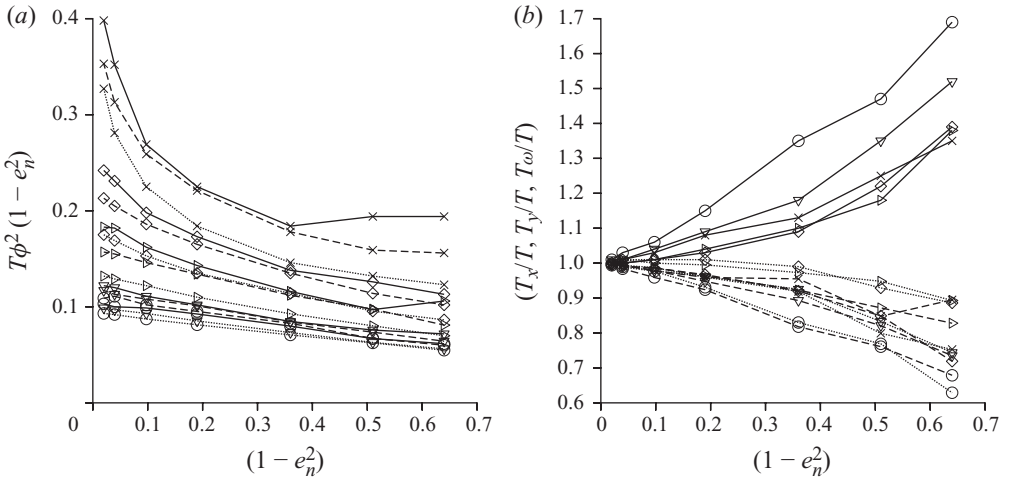

FIGURE 7. The scaled temperature, $T\phi^2(1-e_n^2)$ (a), and the temperature anisotropy (b), as a function of $(1-e_n^2)$ for area fractions $\phi = 0.1$ ($\circ$), $\phi = 0.3$ ($\triangledown$), $\phi = 0.5$ ($\triangleright$), $\phi = 0.6$ ($\diamond$) and $\phi = 0.7$ ($\times$). (a) Solid lines: the results for $(L/D) = 1.0$, dashed lines: the results for $(L/D) = 0.25$ and dotted lines: the results for $L/D = 0.0$ (disks). (b) (T_x/T) (solid lines), (T_y/T) (broken lines) and (T_ω/T) (dotted lines) are shown for $(L/D) = 1.0$.

and nearly elastic collisions, and then present results over a range of area fractions. In a granular flow, the temperature is determined by a balance between the rate of production of energy due to mean shear and the rate of dissipation due to inelastic collisions. The rate of production is proportional to $\mu\dot{\gamma}^2$, where the viscosity μ is $(T^{1/2}/D)$ times a function of e_n, (L/D) and the area fraction. In the limit of low area fraction and nearly elastic collisions, the viscosity is independent of area fraction, and so the rate of production of energy is $(T^{1/2}\dot{\gamma}^2/D)$ times a function of (L/D). The rate of dissipation of energy due to collisions between pairs of particles, in the limit of low area fraction, is $\phi^2(1-e_n^2)T^{3/2}/d^2$ times a function of (L/D) in the near-elastic limit and in the limit of low area fraction. This implies that the temperature should scale as $1/(\phi^2(1-e_n^2))$ times a function of (L/D) in the limit $\phi \to 0$ and $e_n \to 1$. Therefore, we plot $T\phi^2(1-e_n^2)$ as a function of e_n for different area fractions and different aspect ratios in figure 7(a). It is observed that there is very little variation in the scaled temperature with e_n at low area fractions, and the scaled temperature is close to 0.1 when the area fraction is less than about 0.3. However, there is a larger variation for area fractions greater than 0.5. One striking feature in figure 7(a) is that there is very little dependence of the scaled temperature on the aspect ratio. The granular temperature seems to vary only with area fraction and coefficient of restitution, and is independent of (L/D).

The anisotropy in the granular temperature is shown in figure 7(b), where the ratios (T_x/T), (T_y/T) and (T_ω/T) are shown as a function of e_n, where $T_x = \langle v_x'^2 \rangle$, $T_y = \langle v_y'^2 \rangle$ and $T_\omega = I\langle \omega'^2 \rangle$. Only the results for $(L/D) = 1$ are shown in figure 7(b); the qualitative results for other (L/D) ratios are similar, so we do not plot these. Figure 7(b) shows, as expected, that the distribution of fluctuating velocities is nearly isotropic for nearly elastic particles in the limit $e_n \to 1$. In all cases, the fluctuating energy in the translational motion in the x-direction is larger than the average fluctuating energy, while that in the translational motion in the y-direction and in the rotational motion are smaller than the average fluctuating energy. An interesting feature is that the

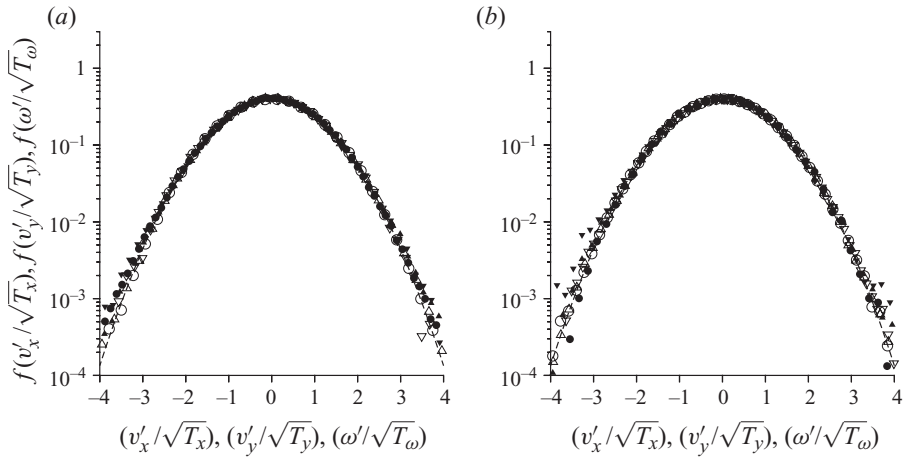

FIGURE 8. The velocity distribution functions $f(v_x'/\sqrt{T_x})$ versus $(v_x'/\sqrt{T_x})(\bigcirc)$, $f(v_y'/\sqrt{T_y})$ versus $(v_y'/\sqrt{T_y})(\triangle)$ and $f(\omega'/\sqrt{T_\omega})$ versus $(\omega'/\sqrt{T_\omega})(\triangledown)$, for $e_n = 0.95$ (open symbols) and $e_n = 0.7$ (filled symbols), and for area fraction $\phi = 0.1$ (a) and $\phi = 0.7$ (b). Broken lines: the Gaussian distribution.

anisotropy in the distribution of fluctuating velocities decreases as the area fraction in increased, except for the highest area fraction of 0.7 studied here. This can be attributed to steric effects; as the area fraction increases, the effectiveness of the collisional mechanism for re-distributing the energy between the different directions increases, and so the anisotropy in the root-mean-square velocities decreases.

The velocity distributions for the translational and rotational velocities are shown at a low area fraction ($\phi = 0.1$) in figure 8(a), and at a relatively high area fraction ($\phi = 0.7$) in figure 8(b). The aspect ratio (L/D) is 1 in both cases, and results are provided both for nearly elastic particles as well as for particles with $e_n = 0.7$. A striking observation from these figures is that the velocity distribution is well approximated by a Gaussian distribution in all cases, even for elongated particles with $(L/D) = 1$, at both high and low area fractions, as well as for relatively inelastic particles with $e_n = 0.7$. The distribution function is a Gaussian for the velocities in the flow and gradient directions, as well as for the angular velocity fluctuations. We do not see any power law or algebraic tails within the limits of resolution in the simulation, and there is also no observable skewness or flatness in the profiles. This is likely to result in significant simplification in the modelling of granular flows of elongated particles, since the distribution functions for the particle-velocity fluctuations can be well modelled by anisotropic Gaussian distributions.

3.3. *Collision frequency*

The collision frequency ν is of significance in a dense granular flow of hard particles, because the transport of momentum and energy due to collisions is large compared to that due to the streaming of particles. At low area fractions, the collision frequency (number of collisions per particle per unit time) in a hard-particle gas is proportional to $\rho D^2\sqrt{T}$ in three dimensions, and proportional to $\rho D\sqrt{T}$ in two dimensions, where ρ is the number density of the particles and D is the characteristic particle size, and the fluctuating velocity is proportional to $\sqrt{T}$. However, as the area fraction increases, the proportionality $\nu \propto \rho\sqrt{T}$ is modified because of excluded area and shadowing effects,

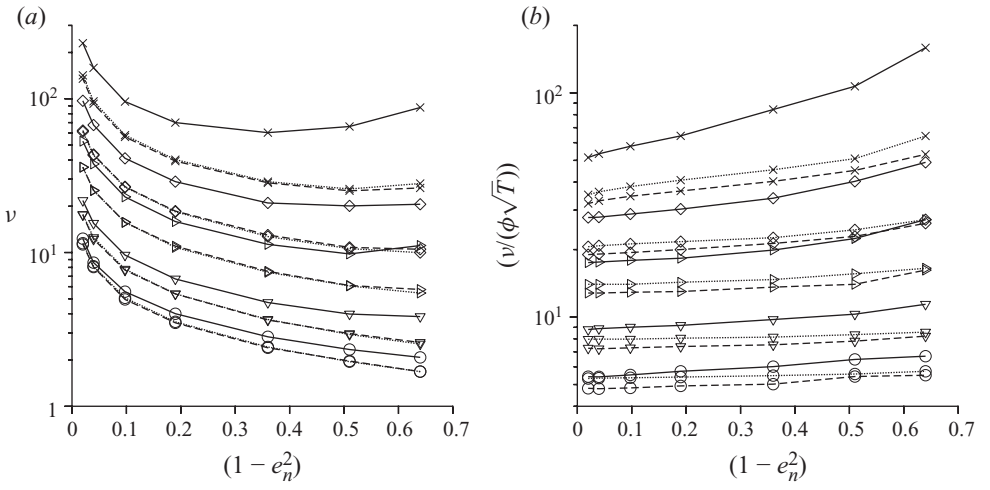

FIGURE 9. The collision frequency ν (a), and the scaled collision frequency $(\nu/\phi\sqrt{T})$ (b), as a function of $(1 - e_n^2)$ for $(L/D) = 1.0$ (solid lines) and $(L/D) = 0.25$ (dashed lines) and $(L/D) = 0.0$ (dotted lines) for area fractions $\phi = 0.1$ ($\circ$), $\phi = 0.3$ ($\triangledown$), $\phi = 0.5$ ($\triangleright$), $\phi = 0.6$ ($\diamond$) and $\phi = 0.7$ ($\times$).

which are not included in the theories for dilute gases. The collision frequency in the dense limit is usually expressed using the pair distribution function, which is effectively the ratio of the actual collision frequency and the collision frequency predicted by kinetic theory in the dilute limit. In the present case, the pair distribution function is more complicated because it depends on the relative orientations of the colliding particles in addition to their relative positions. We do not attempt to calculate the complete pair distribution function in the present analysis, but restrict our attention to analysing the collision frequency.

The variation of the collision frequency, scaled by the strain rate, is shown as a function of the coefficient of restitution for different area fractions and (L/D) ratios in figure 9(a). It is observed that the collision frequency increases as the area fraction increases, due to the excluded area effect. When the area fraction is increased from 0.1 to 0.7, the collision frequency increases by about two orders of magnitude. The collision frequency also increases when the aspect ratio of the particles increases at constant area fraction and as the coefficient of restitution approaches 1. This is because the frequency of inter-particle collisions is due to the velocity fluctuations of the particles and the root mean square of the velocity fluctuations (square root of the temperature) increases as $(1 - e_n^2)^{-1/2}$ at constant strain rate as the coefficient of restitution approaches 1.

An averaged pair distribution function at contact, which is averaged over the relative orientations of the colliding particles, can be defined as the ratio of the actual collision frequency and the collision frequency (proportional to $\phi\sqrt{T}$) predicted by kinetic theory of gases. Therefore, the averaged pair distribution function is proportional to $\nu/(\phi\sqrt{T})$. In figure 9(b), we plot $\nu/(\phi\sqrt{T})$ as a function of the coefficient of restitution at different area fractions. It is observed that this function shows very little variation with the coefficient of restitution, though it does vary as the (L/D) ratio is changed. The variation of $\nu/(\phi\sqrt{T})$ is shown as a function of the area fraction for two different (L/D) values and two different coefficients of restitution in figure 10. It is observed that $\nu/(\phi\sqrt{T})$, which is proportional to the pair distribution

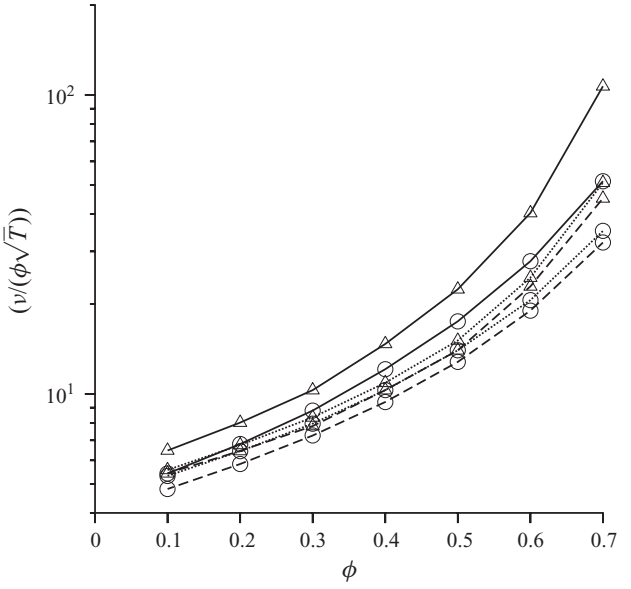

FIGURE 10. The ratio $\nu/(\phi\sqrt{T})$ as a function of area fraction ϕ for $(L/D) = 1.0$ (solid lines), $(L/D) = 0.25$ (dashed lines) and $(L/D) = 0.0$ (dotted lines), and for coefficients of restitution $e_n = 0.9$ (○) and $e_n = 0.7$ (△).

function, increases between one and two orders of magnitude as the area fraction is increased from 0.1 to 0.7. In the case of spherical particles, it has been reported (Kumaran 2004, 2006, 2008, 2009*a*,*b*) that there is a significant increase in the collision frequency scaled by the square root of temperature at high volume fractions. This is due to correlations in the velocities of colliding particles, because of which the relative velocity distribution is closer to an exponential distribution instead of a Gaussian distribution for elastic particles. A similar increase is observed in the present case as well.

3.4. *Stress tensor*

The stress tensor is calculated as follows by summing the tensor product of the impulse transmitted and the distance between the centres of the dumbbells in an area A (in two dimensions) over a time interval τ, and dividing by the time interval and the volume:

$$\boldsymbol{\sigma} = \frac{1}{\tau A} \sum_{\text{collisions}} (\Delta \boldsymbol{p})(\Delta \boldsymbol{x}), \tag{3.6}$$

where V is the total volume of the system, τ is the time interval over which the stress tensor is calculated, $\Delta \boldsymbol{p}$ is the impulse from (2.2) and $\Delta \boldsymbol{x}$ is the vector displacement between the centres of the two dumbbells (not the distance between the centres of the two colliding disks). All components of the stress are scaled by the particle mass, since the particle mass is considered to be 1 in the simulations. Since the stress is a force per unit length in two dimensions, the stress does not contain any length dimension. Since the collisions are instantaneous in the system considered here, there is no material time scale. Therefore, all components of the stress are proportional to $\dot{\gamma}^2$.

We set the strain rate equal to 1 without loss of generality, so that all time scales are non-dimensionalized by the inverse of the strain rate. Therefore, the stress tensor

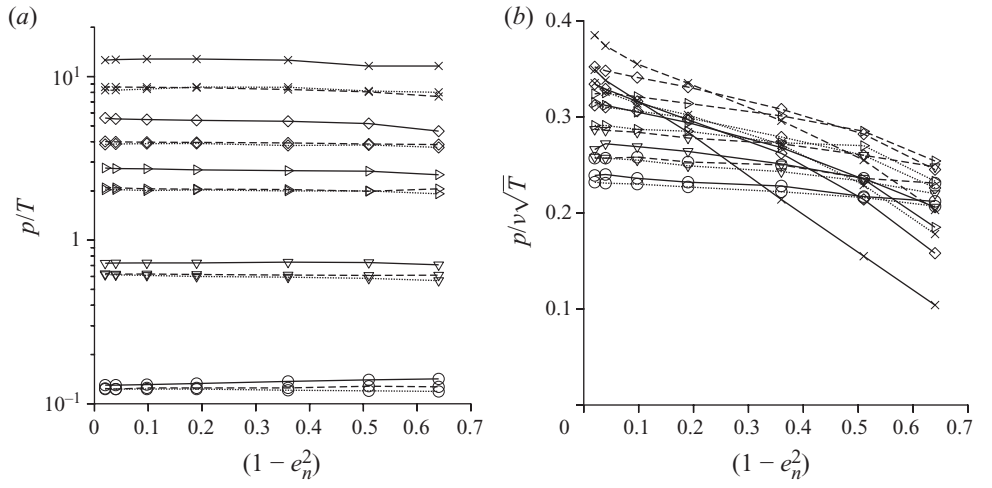

FIGURE 11. The ratio of pressure and temperature (p/T) (a) and the ratio $(p/\nu\sqrt{T})$ (b) as a function of $(1-e_n^2)$ for $(L/D)=1.0$ (solid line), $(L/D)=0.25$ (dashed line) and $(L/D)=0.0$ (dotted line), and for area fractions $\phi=0.1$ ($\bigcirc$), $\phi=0.3$ ($\triangledown$), $\phi=0.5$ ($\triangleright$), $\phi=0.6$ ($\diamond$) and $\phi=0.7$ ($\times$).

is only a function of the aspect ratio, area fraction and coefficient of restitution. When scaled by the square of the strain rate, the pressure diverges as $e_n \to 1$. This is because the temperature, which is proportional to $\dot{\gamma}^2 D^2/(1-e_n^2)$ from energy balance, diverges for $e_n \to 1$ at fixed strain rate. Therefore, it is preferable to analyse the variation of the scaled pressure (p/T), as shown in figure 11(a), where $p=(\sigma_{xx}+\sigma_{yy})/2$, with $(1-e_n^2)$ for two different aspect ratios and for different area fractions. This graph shows that the ratio of pressure and temperature is nearly independent of coefficient of restitution over a range $e_n=0.99$–0.7, and the ratio depends only on the aspect ratio and the area fraction. In order to place this result in context, we note that for a hard-particle elastic fluid, there is no intrinsic energy scale for particle interactions, and so the pressure is a product of the temperature and a function of the area fraction and aspect ratio. We would expect, by extension, that for the present system of inelastic particles, the pressure would be the product of the temperature and some function of the area fraction, aspect ratio and coefficient of restitution. Figure 11(a) shows that this function has almost no dependence on the coefficient of restitution, and so the equation of state (relation between temperature and pressure) for inelastic dumbbells is numerically almost identical to that for a system of elastic dumbbells.

An averaged equation of state for the pressure as a function of the temperature can be obtained by averaging the p/T values for different coefficients of restitution, and then plotting this as a function of (L/D) and area fraction. This averaged equation of state is shown as a function of area fraction for different (L/D) values in figure 12. The ratio does show a significant increase with area fraction, especially in the limit of high area fractions, but it does not vary much with the (L/D) for all the aspect ratios considered here.

In the limit of high area fraction, it is more appropriate to define a scaled pressure as $p/\nu\sqrt{T}$. This is because the collisional mechanism is the dominant mechanism of momentum transport, and the momentum flux is proportional to the collision frequency and the fluctuating velocity, because the average impulse in a collision scales as the mass times the fluctuating velocity. In figure 11(b), the ratio $p/\nu\sqrt{T}$ is

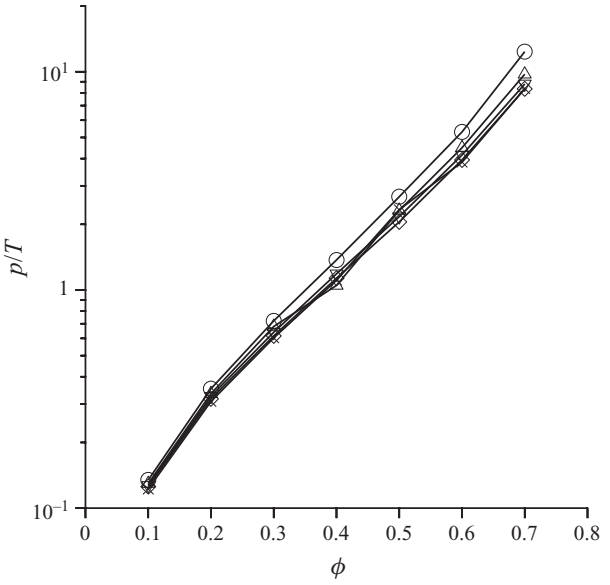

FIGURE 12. The ratio of pressure and temperature p/T as a function of area fraction for $(L/D) = 1.0$ (○), $(L/D) = 0.75$ (△), $(L/D) = 0.5$ (▽), $(L/D) = 0.25$ (◇) and $(L/D) = 0$ (×).

shown as a function of the coefficient of restitution for two different (L/D) ratios and for different area fractions. It is clearly seen that the variation of the scaled pressure $p/\nu\sqrt{T}$ is small compared to that of the pressure itself, especially in the limit of high area fraction. It is seen that this ratio varies in a very narrow range, between about 0.1 and 0.4, for all the area fractions and coefficients of restitution considered here, even when the pressure varies by one to two orders of magnitude in figure 11. The ratio $p/(\nu\sqrt{T})$ increases with area fractions for nearly elastic particles; however, at coefficients of restitution less than about 0.8, this ratio first increases and then decreases with area fraction. The decrease in $(p/(\nu\sqrt{T}))$ at higher area fractions is possibly because of ordering of particles and the decrease in the magnitude of the mean angular velocity, as discussed a little later. It should be noted that for non-circular particles, collisions can be induced both by the translational and the rotational motion of the particles, and the effect of particle rotation is likely to become more important as the particles are more densely packed. Therefore, the collision frequency will decrease when the mean angular velocity decreases. The effect of rotation is also more important as the aspect ratio increases. For this reason, we observe that $(p/(\nu\sqrt{T}))$ decreases as the aspect ratio increases as the coefficient of restitution is decreased, where there is an increase in the orientational order parameter and the magnitude of the mean angular velocity decreases.

The ratio of the shear stress and the pressure, σ_{xy}/p, is shown as a function of $(1 - e_n^2)$ for different aspect ratios and area fractions in figure 13(a). This figure shows that there is very little variation in the ratio σ_{xy}/p with either area fraction or aspect ratio, and the ratio of shear stress and pressure varies in a very narrow range for all the values of area fraction and aspect ratio considered here. It is also observed that σ_{xy}/p goes to zero as $e_n \to 1$. This can be explained as follows. The shear stress is the product of the viscosity and the strain rate, and the viscosity is proportional to $\sqrt{T}$ at fixed area fraction and aspect ratio. Therefore, the shear stress is proportional to $\sqrt{T}\dot{\gamma}$. Since the pressure is proportional to T at fixed aspect ratio

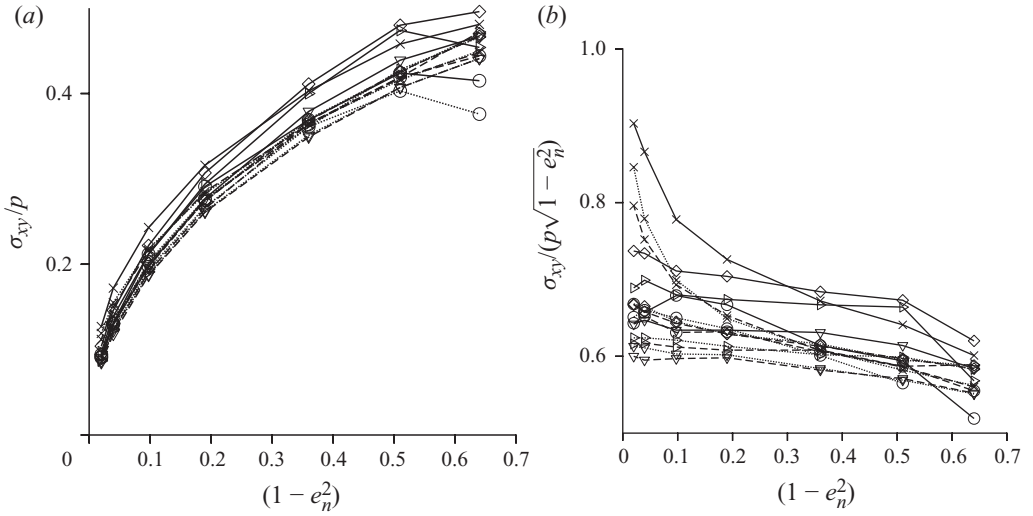

FIGURE 13. The ratio of shear stress and pressure (σ_{xy}/p) (a), and the quantity ($\sigma_{xy}/(p(1-e_n^2))$) (b), as a function of $(1-e_n^2)$ for $(L/D) = 0.0$ (solid line), $(L/D) = 0.25$ (dashed line) and $(L/D) = 1.0$ (dotted line), and for area fractions $\phi = 0.1$ ($\circ$), $\phi = 0.3$ ($\triangledown$), $\phi = 0.5$ ($\triangleright$) and $\phi = 0.7$ ($\times$).

and area fraction, the ratio of the shear stress and the pressure is proportional to $D\dot{\gamma}/\sqrt{T}$, which is proportional to $\sqrt{1-e_n^2}$ from energy balance. Therefore, the ratio of the shear stress and pressure is proportional to $\sqrt{1-e_n^2}$ for $e_n \to 1$. Figure 13(b) shows $\sigma_{xy}/(p\sqrt{1-e_n^2})$. As expected on the basis of the above arguments, this ratio approaches a constant value for $e_n \to 1$, and it varies in a small range from about 0.6 to 0.8 for all area fractions in the range $\phi = 0.1$ to $\phi = 0.7$, and for all aspect ratios considered here.

The first normal stress difference, $(\sigma_{xx} - \sigma_{yy})/p$, shown as a function of $(1-e_n^2)$ for different aspect ratios and area fractions in figure 14(a), is positive for small area fractions, and it is numerically large, indicating that the normal stresses in the flow direction is significantly larger than the normal stress in the gradient direction at low area fractions. As the area fraction increases, the normal stress difference becomes numerically small, and it becomes negative for larger values of (L/D). The normal stress difference decreases with an increase in area fraction because the collisional mechanism of momentum transport becomes dominant, and this mechanism tends to equalize velocity fluctuations in the different directions. An increase in aspect ratio does result in an increase in the normal stress difference at low area fractions, but this difference becomes smaller as the area fraction is increased. Therefore, for very dense flows of aspherical granular materials, it is a good approximation to consider the pressure to be isotropic. As the area fraction is reduced, an isotropic pressure is not a good approximation for low coefficients of restitution.

An important issue for particles with a rotational degree for freedom is whether the stress tensor is symmetric. This is examined in figure 14(b), where the difference in the off-diagonal components $(\sigma_{xy} - \sigma_{yx})$, divided by the average value of the off-diagonal components, $(\sigma_{xy} + \sigma_{yx})/2$, is shown as a function of $(1-e_n^2)$, for $(L/D) = 1$ and for different area fractions. This figure shows that the difference in the off-diagonal components is numerically small compared to the shear stress. For averages carried out over 500 configurations with 216 particles each, we would expect a fluctuation of

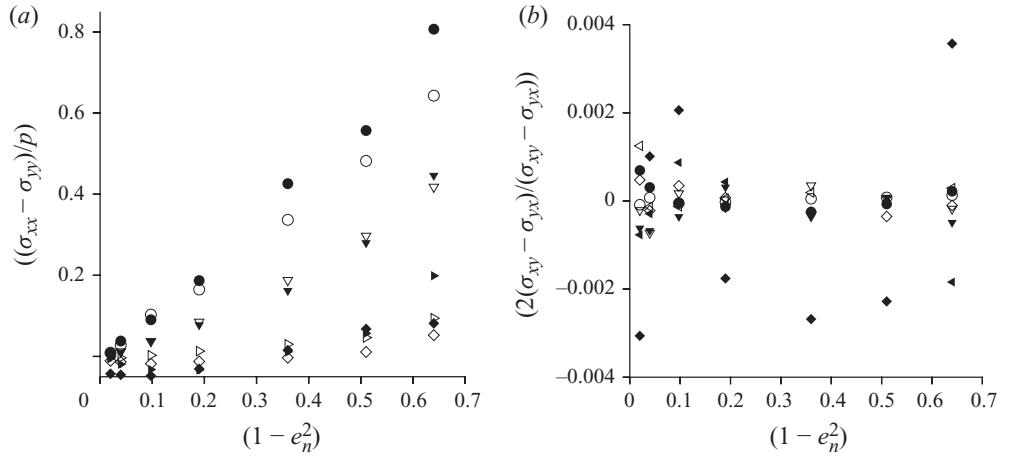

FIGURE 14. The first normal stress difference $(\sigma_{xx}-\sigma_{yy})/p$ (a), and the scaled antisymmetric part of the rate of deformation tensor $(2(\sigma_{xy}-\sigma_{yx})/(\sigma_{xy}+\sigma_{yx}))$ (b), as a function of $(1-e_n^2)$ for $(L/D)=1.0$ (filled symbols) and $(L/D)=0.25$ (open symbols), and for area fractions $\phi=0.1$ ($\circ$), $\phi=0.3$ ($\triangledown$), $\phi=0.5$ ($\triangleright$) and $\phi=0.7$ ($\diamond$).

about 0.3 % from the central limit theorem. The fluctuations in the antisymmetric part of the rate of deformation tensor are well within this range, as shown in figure 14(b). Therefore, we can conclude that the stress tensor is symmetric in our system. This is expected, because we are considering a steady flow, and there are no microscopic torques on the particles.

3.5. *Dissipation rate*

Since we are considering a steady flow, the rate of dissipation of energy is equal to $\mu\dot{\gamma}^2$, where μ is the viscosity and $\dot{\gamma}$ is the strain rate. It is appropriate to define a scaled rate of dissipation of energy in the low-area-fraction limit as $D'=\mu\dot{\gamma}/(1-e_n^2)\phi^2T^{3/2}$, since the decrease in energy in a collision is proportional to $(1-e_n^2)$ times the square of the fluctuating velocity (T), while the frequency of collisions per unit area is proportional to $\phi^2\sqrt{T}$. In the limit of high area fractions, the scaled rate of dissipation of energy per unit area can be defined as $D''=\mu\dot{\gamma}/(1-e_n^2)\nu T\phi$, since the frequency of collisions is ν, while the energy dissipation in a collision is proportional to $(1-e_n^2)\sqrt{T}$. The rate of dissipation of energy, non-dimensionalized in these two ways, is shown as a function of $(1-e_n^2)$ for different aspect ratios and area fractions in figure 15. It is observed that there is a significant variation of the scaled dissipation rate D' with $(1-e_n^2)$ and with area fraction over the range of area fractions considered here. However, the scaled dissipation rate D'' shows very little variation with area fraction and coefficient of restitution, indicating that the collision frequency is the relevant dynamical quantity that determines the dissipation rate in the system. The scaled dissipation rate D'' is nearly a constant for nearly elastic particles, but decreases significantly as the coefficient of restitution decreases below about 0.8. In the case of spherical particles, it has been reported (Kumaran 2009*a*,*b*) that there is a decrease in the dissipation rate scaled by the collision frequency at high volume fractions because of correlations in the velocities of colliding particles; due to correlations, the relative velocity distribution is closer to an exponential distribution instead of a Gaussian distribution for elastic particles. Though we have not explicitly calculated the relative velocity distributions here, the graph of D'' versus coefficient of restitution

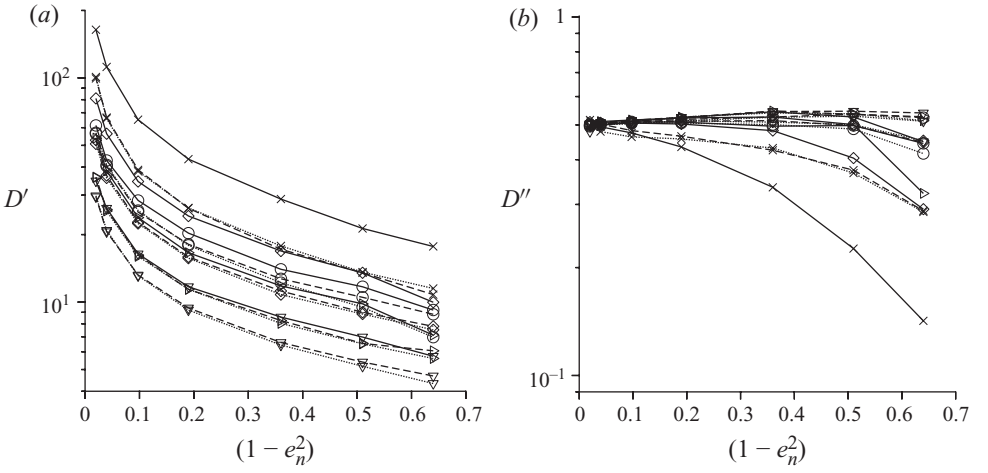

FIGURE 15. The scaled dissipation rate, $D' = (\sigma_{xy}\dot{\gamma}/((1-e_n^2)\phi^2 T^{3/2}))$ (a), and $D'' = (\sigma_{xy}\dot{\gamma}/((1-e_n^2)\phi\nu T))$ (b), as a function of of $(1-e_n^2)$ for $(L/D) = 0.0$ (dashed line), $(L/D) = 0.25$ (broken line) and $(L/D) = 1.0$ (solid line), and for area fractions $\phi = 0.1$ ($\bigcirc$), $\phi = 0.3$ ($\triangledown$), $\phi = 0.5$ ($\triangleright$) and $\phi = 0.7$ ($\times$).

indicates that a similar phenomenon is present in the case of non-circular particles as well.

3.6. *Angular velocity*

An important quantity of interest is the mean angular velocity of the particles. Figure 14(b) shows that the stress tensor is always symmetric. In this case, continuum Cosserat theories (Mitarai, Hayakawa & Nakanishi 2002; Mohan, Nott & Rao 2002) predict that the rate of rotation of the individual particles has to be equal to the rate of rotation of the material elements. This implies that the angular velocity of the particles has to be equal to half the vorticity. If the angular velocity of the particles is equal to the local mean rate of rotation of the fluid, then the mean particle angular velocity has to be equal to half the local vorticity. In the present case, the mean angular velocity of the particles should be equal to -0.5, because we have considered the strain rate to be equal to 1 and anticlockwise rotation is considered positive. The mean angular velocity across the channel is shown as a function of the coefficient of restitution for $(L/D) = 1$ and for different area fractions in figure 16. Although there are large error bars for $e_n \to 1$ and for low area fractions, it is observed that the mean angular velocity is close to -0.5, which is expected if the angular velocity of the particles is equal to the mean rotation rate of the fluid. For highly inelastic particles, the magnitude of the mean angular velocity even appears to increase above 0.5, though a definitive inference cannot be drawn due to the larger error bars at low area fractions. However, at area fractions higher than about 0.4, it is clearly observed that the magnitude of the mean angular velocity decreases below 0.5. This implies that the rate of rotation of the particles is different from, and slower than, the mean local rate of rotation of the fluid.

In figure 14(b), we find that the stress tensor is symmetric, and the antisymmetric part of the stress tensor is equal to zero within the numerical accuracy of the simulations. This implies that there is no local torque acting on the particles. Despite this, the mean angular velocity of the particles is different from the mean rotation in the fluid even when there is no torque on the particles. This indicates that the shear

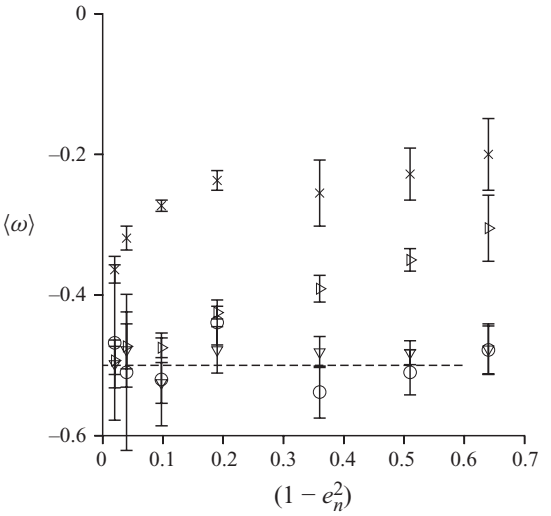

FIGURE 16. Mean angular velocity as a function of $(1 - e_n^2)$ for $(L/D) = 1$, and for $\phi = 0.1$ (○), $\phi = 0.3$ (▽), $\phi = 0.5$ (▷) and $\phi = 0.7$ (×).

flow of inelastic dumbbells cannot be described by micro-polar theories for Cosserat continua (Mitarai *et al.* 2002; Mohan *et al.* 2002). This is probably because there is a distinct average orientation direction in the flow, which is the principal axis of the orientation tensor for the dumbbells. This is probably because of steric hindrance effects, which restrict rotational motion of the particles. However, these effects do not reduce the angular velocity to zero; the angular velocity is still non-zero, but about half the value expected if it were a Cosserat continuum.

4. Conclusions

We have studied the dynamics and structure of a system of inelastic dumbbells in a linear shear flow using an ED simulation technique using Lees–Edwards boundary conditions. The presence of the orientational degree of freedom makes the simulation procedure considerably more complicated than is the case for spherical particles. We use the method of retrospective collision detection. The collision between a pair of dumbbells, which is instantaneous, is characterized by a normal coefficient of restitution, e_n that is equal to 1 for elastic collisions and is less than 1 for inelastic collisions. The relative velocity tangential to the surfaces of contact is unchanged in a collision.

4.1. *Granular temperature*

In equilibrium systems, the velocity fluctuations in different degrees of freedom are, by the equipartition theorem, equal. In inelastic systems, equipartition does not apply, so it is necessary to consider a granular temperature for each degree of freedom. In the two-dimensional dumbbell system, there are three temperatures: T_x, T_y and T_ω, corresponding to velocity fluctuations in the flow direction, the gradient direction and the angular velocity, respectively. As expected, for nearly elastic particles the three granular temperatures are almost equal. As the inelasticity increases we observe that $T_x > T_y > T_\omega$. At high packing fractions, the difference between the energies of translational and rotational motion is not more than 10 %, implying that the approximation of assuming equipartition is reasonable. This is due to the greater

collisional efficiency of the redistribution of energy between the different degrees of freedom at higher packing fraction. We also observed that the overall granular temperature, $(T_x + T_y + T_\omega)/3$, varies only slightly with the aspect ratio (L/D).

A surprising observation, which has the potential to simplify the development of kinetic theories for non-spherical inelastic particles, is that the distributions of translational and rotational velocities are all Gaussian to a very good approximation.

4.2. *Stress and dissipation rate*

The ratio of the pressure to the temperature, p/T, is nearly independent of the coefficient of restitution, and shows some variations with the aspect ratio (L/D). This is a significant result and it will be interesting to see if it extends to other types of particles. Also significant is that the ratio $p/(\nu\sqrt{T})$ shows little variation over the entire range of area fraction and coefficient of restitution studied here. Similarly, we found that the scaling $\sigma_{xy}\dot{\gamma}/((1-e_n^2)\phi\nu T)$ for the scaled dissipation rate, appropriate for high area fractions, results in a greater collapse of the data than the scaling $\sigma_{xy}\dot{\gamma}/((1-e_n^2)\phi^2 T^{3/2})$ (appropriate in the low packing fraction limit). This indicates that collisional transport is the dominant mechanism of stress transmission, even at the lowest area fraction.

The collision frequency, pressure and shear stress all increase as the aspect ratio (L/D) is increased form 0.0 to 1.0. However, the maximum increase in the collision frequency is about a factor of 2 at the highest area fraction of 0.7, while the increase in the pressure and stress is smaller. This is in contrast to the increase of an order of magnitude or more when the volume fraction is increased from 0.1 to 0.7. This leads us to the conclusion that an accurate modelling of the shape of the particles is important for predicting the stresses, but approximate estimates can be obtained using theories for isotropic particles; the volume fraction seems to have a much greater influence on the stresses than the shape.

4.3. *Mean angular velocity*

Unlike the density, mean velocity and the stress, the mean angular velocity displays significant fluctuations across the channel. This may be due to long-lived correlations in the particle rotation rate, which requires further study. Despite the large error bars, however, some clear trends were visible. The mean angular velocity is equal to -0.5 for low area fraction and coefficients of restitution close to 1. This is the expected result if the particle angular velocity is equal to the local rate of rotation of the fluid. At higher packing fraction, however, the mean angular velocity is less than half the local vorticity. This indicates that the flow of anisotropic particles cannot be described by micro-polar theories for Coserrat continua, and it is necessary to incorporate particle orientation as a separate field.

This research was supported by the J. C. Bose Fellowship, Department of Science and Technology, Government of India. Support in the form of a visiting Professor position for J. T. at the Indian Institute of Science is gratefully acknowledged.

REFERENCES

Allen, M. P., Frenkel, D. & Talbot, J. 1989 Molecular dynamics simulation using hard particles. *Comput. Phys. Rep.* **9**, 301.

Aranson, I. S., Snezhko, A., Olafsen, J. S. & Urbach, J. S. 2008 Comment on 'Long-Lived Giant Number Fluctuations in a Swarming Granular Nematic'. *Science* **320**, 612c.

Bertrand, F., Leclaire, L. A. & Levecque, G. 2005 DEM-based models for the mixing of granular materials. *Chem. Engng Sci.* **60**, 2517–2531.

Blair, D. L., Neicu, T. & Kudrolli, A. 2003 Vortices in vibrated granular rods. *Phys. Rev.* E **67**, 031303–031308.

Cleary, P. W. 2008 The effect of particle shape on simple shear flows. *Powder Technol.* **179**, 144–180.

Cleary, P. W. & Sawley, O. D. L. 2002 DEM modelling of industrial granular flows: 3D case studies and the effect of particle shape on hopper discharge. *Appl. Math. Model.* **26**, 85–111.

Cole, D. M. & Peters, J. F. 2007 A physically based approach to granular media mechanics: grain-scale experiments, initial results and implications to numerical modeling. *Granular Matter* **9**, 309–321.

Cole, D. M. & Peters, J. F. 2008 Grain-scale mechanics of geologic materials and lunar simulants under normal loading. *Granular Matter* **10**, 171–185.

Cundall, P. A. & Strack, O. D. L. 1979 A discrete numerical model for granular assemblies. *Geotechnique* **29**, 47–65.

Galanis, J., Harries, D., Sackett, D. L., Losert, W. & Nossal, R. 2006 *Phys. Rev. Lett.* **96**, 028002.

Gallas, J. A. C. & Sokolowski, S. 1993 Grain non-sphericity effects on the angle of repose in a granular material. *Intl J. Mod. Phys.* B **7**, 2037–2046.

Kumaran, V. 2004 Constitutive relations and linear stability of a sheared granular flow. *J. Fluid Mech.* **506**, 1–43.

Kumaran, V. 2006 The constitutive relations for the granular flow of rough particles, and its application to the flow down an inclined plane. *J. Fluid Mech.* **561**, 1–42.

Kumaran, V. 2008 Dense granular flow down an inclined plane – from kinetic theory to granular dynamics. *J. Fluid Mech.* **599**, 120–168.

Kumaran, V. 2009*a* Dense sheared granular flows. Part I. Structure and diffusion. *J. Fluid Mech.* **632**, 109–144.

Kumaran, V. 2009*b* Dense sheared granular flows. Part II. The relative velocity distribution. *J. Fluid Mech.* **632**, 145–198.

Langston, P. A., Al-Awamleh, M. A., Fraige, F. Y. & Asmar, B. M. 2004 Distinct element modelling of non-spherical frictionless particle flow. *Chem. Engng Sci.* **59**, 425–435.

Lees, A. W. & Edwards, S. F. 1972 *J. Phys.* C **5**, 1921.

Lumay, G. & Vandewalle, N. 2004 Compaction of anisotropic granular materials: Experiments and simulations. *Phys. Rev.* E **70**, 051314.

Matuttis, H. G. 1998 Simulations of the pressure distribution under a two dimensional heap of polygonal particles. *Granular Matter* **1**, 83–91.

Mitarai, N., Hayakawa, H. & Nakanishi, H. 2002 Collisional Granular flow as a Micropolar fluid. *Phys. Rev. Lett.* **88**, 174–301.

Mohan, L. S., Nott, P. R. & Rao, K. K. 2002 A frictional Cosserat model for the slow shearing of granular materials. *J. Fluid Mech.* **457**, 377–409.

Narayan, V., Ramaswamy, S. & Menon, N. 2007 *Science* **317**, 105.

Pena, A. A., Garcia-Rojo, R. & Herrmann, H. J. 2007 Influence of particle shape on sheared dense granular media *Granular Matter* **9**, 279–291.

Poschel, T. & Buchholtz, V. 1995 Molecular dynamics of arbitrarily shaped granular particles. *J. Phys. France* **5**, 1431–1445.

Rebertus, W. & Sando, K. M. 1977 Molecular dynamics simulation of a fluid of hard spherocylinders. *J. Chem. Phys.* **67**, 2585–2590.

Reddy, K. A., Kumaran, V. & Talbot, J. 2009 Orientational ordering in sheared inelastic dumbbells. *Phys. Rev.* E **80**, 031304.

Stokely, K., Diacou, A. & Franklin, S. V. 2003 Two-dimensional packing in prolate granular materials. *Phys. Rev.* E **67**, 051302.

Villarruel, F., Lauderdale, B., Mueth, D. M. & Jaeger, H. M. 2000 Compaction of rods: relaxation and ordering in vibrated, anisotropic granular material. *Phys. Rev.* E **61**, 6914–6919.

Zhu, H. P., Zhou, Z. Y., Yang, R. Y. & Yu, A. B. 2007 Discrete particle simulation of particulate systems: theoretical developments. *Chem. Engng Sci.* **62**, 3378–3396.